

Comparison of Inviscid and Viscous Aerodynamic Predictions of Supersonic Retropropulsion Flowfields

Ashley M. Korzun¹, Christopher E. Cordell, Jr.², and Robert D. Braun³
Georgia Institute of Technology, Atlanta, GA, 30332

Supersonic retropropulsion, or the initiation of a retropropulsion phase at supersonic freestream conditions, is an enabling decelerator technology for high-mass planetary entries at Mars. The current knowledge on supersonic retropropulsion is largely derived from exploratory development efforts prior to the Viking missions in the 1960s and early 1970s, predominantly sub-scale wind tunnel testing. Little literature exists on analytical and computational modeling approaches for supersonic aerodynamic-propulsive interactions at moderate thrust levels and flight-relevant conditions. This investigation presents a discussion of the relevant flow physics to provide insight into the effectiveness of inviscid and viscous computational analysis approaches in consistently and accurately capturing the relevant flow physics. Preliminary computational results for a blunt body with two retropropulsion configurations are compared with experimental data for the location of prominent flow features and surface pressure distributions. This work is intended to provide an initial discussion of the challenges facing the computational simulation of supersonic retropropulsion flowfields.

Nomenclature

A	=	area, m ²
C_p	=	pressure coefficient
C	=	force coefficient
D	=	diameter, m
M	=	Mach number
p	=	pressure, N/m ²
q	=	dynamic pressure, N/m ²
Re	=	Reynolds number
r	=	radius, m
T	=	thrust, N
$T_{0,\infty}$	=	freestream total temperature, K
$T_{0,j}$	=	jet total temperature, K
V	=	velocity, m/s
x	=	axial location, m
α	=	angle of attack, deg
β	=	hypersonic ballistic coefficient, kg/m ²
δ	=	thickness, m
γ	=	ratio of specific heats
φ	=	angular location, deg

Subscripts / Superscripts

a	=	local ambient condition
D	=	body diameter
e	=	nozzle exit

¹ Graduate Research Assistant, Daniel Guggenheim School of Aerospace Engineering, AIAA Student Member.

² Graduate Research Assistant, Daniel Guggenheim School of Aerospace Engineering, AIAA Student Member.

³ David and Andrew Lewis Associate Professor of Space Technology, Daniel Guggenheim School of Aerospace Engineering, AIAA Fellow.

j	= jet condition
m	= model
T	= thrust
∞	= freestream condition
0	= total condition
$*$	= nozzle throat

I. Introduction

THE United States first landed on the surface of Mars in 1976 with Viking 1 and 2.¹ At the present time, four additional landings on Mars have successfully been achieved, with each entry system relying heavily on the entry, descent, and landing (EDL) technologies developed for the Viking missions. Including the 2011 Mars Science Laboratory mission, the largest payload mass among these missions is ~ 1 t. The applicability of these heritage EDL systems, namely blunt body aeroshells, supersonic parachutes, and subsonic, propulsive terminal descent, to the high-mass planetary entries required for the advanced robotic (> 2 t) and human exploration (20 – 100 t) of Mars has been shown to be limited by the physical performance of these systems through the Martian atmosphere.¹ In particular, these missions require unacceptable deployment and operating conditions for supersonic parachutes as a result of high ballistic coefficients, aeroshell size constraints, and insufficient atmospheric density.¹ A number of studies¹⁻⁹ have explored the initiation of a retropropulsion phase at supersonic conditions, or supersonic retropropulsion (SRP), in serial with or in place of a deployable aerodynamic decelerator, to enable the landing of larger payloads on Mars. These studies have recommended investment by NASA in SRP technology.^{1,3,7,9,10}

Much of the current knowledge about supersonic retropropulsion is based on exploratory development efforts prior to the Viking missions in the 1960s and early 1970s.⁸ Results from sub-scale wind tunnel testing during this time show varying degrees of preservation of the vehicle's static aerodynamic drag to be possible at low to moderate thrust levels for peripheral retropropulsion configurations, with the degree of aerodynamic drag preservation strongly dependent on the location of the nozzles on the aeroshell forebody and the relative strength of the exhaust flow to the freestream.⁸ The thrust coefficient, C_T (defined in Eq. (1)), is the most common parameter used to characterize the static aerodynamics and, to a lesser extent, the flowfield stability of the aerodynamic-propulsive interaction. In the context of SRP, C_T is a force coefficient and not a direct function of the nozzle geometry.

$$C_T = \frac{T}{q_\infty A} \quad (1)$$

Recent efforts^{2-7,9} have examined entry systems relying on SRP to establish performance requirements and operating conditions for future mission applications. Thrust coefficients less than ~ 5 are not realistic for any mission class as a result of the large thrust magnitudes required for mass-optimal propulsion system performance. For conservatively sized propulsion systems, initiation conditions range from Mach 1.8 to 3.6 at 5 to 7 km altitude. No reliance on drag preservation (i.e. no operation at conditions corresponding to possible drag preservation) was observed for systems with $\beta = 200$ to 600 kg/m².⁹

Fundamentally, supersonic retropropulsion is characterized by the interaction between the shock layer of the entry vehicle and the retropropulsion exhaust flow.⁸ In the literature, C_T is often used in place of total pressure ratio where the freestream conditions are fixed. Although the majority of the literature is concentrated on wind tunnel test results, several investigations into the capabilities of modern computational analysis tools in simulating similar flow interactions have been completed.¹⁰⁻¹⁸ Most of this computational work focuses on the mitigation of several aerothermal environments during entry or drag reduction for entry vehicles. However, the similarities between the flow interactions across these works are useful for extending the work to analyses targeting drag preservation and augmentation applications for entry. In general, accurate prediction of the static aerodynamics and flowfield stability of blunt body aeroshells with supersonic retropropulsion using computational fluid dynamics (CFD) methods requires the ability to capture detached shocks, shock-shock interactions, recirculation, shock-induced boundary layer separation, and under-expanded and highly under-expanded jet flow structures.

The work presented here uses FUN3D, a NASA-developed CFD tool, to initiate investigation into the ability of inviscid and viscous analysis approaches to consistently and accurately capture the relevant flow physics of the aerodynamic-propulsive interactions arising from supersonic retropropulsion. Complementing a discussion on

supersonic retropropulsion flow physics, computational results for a central and a peripheral retropropulsion configuration are compared with data from a wind tunnel test series completed by Jarvinen and Adams¹¹ in 1970, the only known reference for a peripheral SRP configuration.⁸ This assessment is completed by comparing the location and formation of primary flowfield features and surface pressure distributions with experimental data in a Mach 2.0 freestream. This work seeks to serve as a starting point for understanding the challenges facing the computational simulation of SRP flowfields and presents preliminary FUN3D solutions at relevant conditions.

II. Supersonic Retropropulsion Flow Physics

The supersonic retropropulsion flowfield is a complex interaction between a typically highly under-expanded jet and a directly, or nearly directly, opposing supersonic freestream. SRP plume physics are similar to those for sonic and supersonic jets exhausting into a quiescent medium, and similar extensions can be made from supersonic impinging jets. From the relevant flow physics, predictions of the capabilities of various analysis approaches (inviscid, laminar, turbulent) can be made.

A. Blunt Bodies in Supersonic Flow

Relevant supersonic conditions for SRP are considered to be fully within the continuum flow regime. As shown in Figure 1, the flowfield surrounding a blunt body entry vehicle at supersonic freestream conditions is characterized by a strong, detached shock.¹⁹ To compare relative thicknesses of the bow shock, boundary layer, and shock layer, Gnoffo¹⁹ defines Re_D to be the post-shock Re based on the body diameter of the entry vehicle. The bow shock is very thin, with a non-dimensional thickness, $\delta_1/D \sim Re_D^{-1}$. The boundary layer thickness is greater than the bow shock thickness, with $\delta_2/D \sim Re_D^{-1/2}$. The shock layer includes the boundary layer and extends to the bow shock. The dimensionless thickness in the stagnation region, δ_3/D , is nearly independent of Re_D and instead, controlled by the mass flow rate across the bow shock.¹⁹ For entry vehicles with shallow aftbodies, large flow turning angles, and at small angles of attack, such as the blunt body geometries considered here, the boundary layer may separate behind the shoulder. The separated shear layers converge aft of the body, forming a viscous wake cone.¹⁹

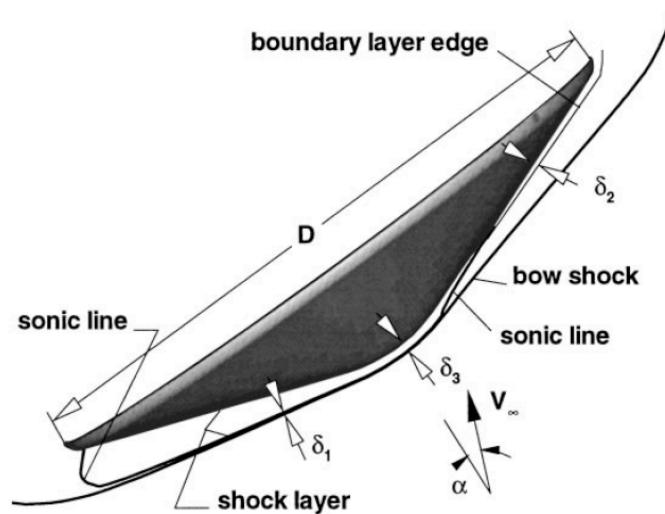


Figure 1. Simplified flowfield over a blunt body entry vehicle.¹⁹

B. Highly Under-expanded Jet Flows

Three expansion conditions are considered for jet flows: over-expanded, under-expanded, and highly under-expanded. Over-expanded jet flows have a lower static pressure at the nozzle exit, p_e , as compared to the local ambient pressure, p_a . For under-expanded jet flows, the static pressure at the nozzle exit is higher than the local ambient pressure, with the ambient pressure indicated in Figure 2. For, highly under-expanded jet flows, p_e is 3–4 times (or more) greater than p_a with supersonic nozzles. In general, highly under-expanded jet flows exhausting from a body into a quiescent medium are characterized by an expansion fan bounded by a barrel shock and terminating with a Mach disk.^{20–24} Figure 2 illustrates the general jet structure. From the nozzle exit, the jet flow undergoes Prandtl-Meyer expansion until the jet pressure equals the local ambient pressure, defining a high-velocity jet boundary. The constant pressure condition at the jet boundary causes the boundary to tend back toward the

centerline of the jet.²¹ A barrel shock is formed as a result of the jet flow being turned at the jet boundary. At highly under-expanded conditions, a Mach reflection occurring within the jet forms a Mach disk.

At the intersection of the Mach disk and the barrel shock, or triple point, an oblique reflected shock forms. This intersecting structure is thought to arise from the formation of a sonic throat-like region allowing the subsonic jet core downstream of the Mach disk to be supersonic on the side of the Mach disk nearer the nozzle exit.²⁵ For jet flows exhausting exclusively into static, quiescent mediums, this theory is analogous to the Mach disk forming where a normal shock has sufficient strength to equate the static pressure behind the shock to the local ambient pressure.²⁵ Jet flow passing through the Mach disk becomes subsonic, while jet flow passing through the barrel shock and oblique reflected shock remains supersonic, resulting in a slip line defining the boundary between the subsonic jet core and the inner, subsonic shear layer.²⁰

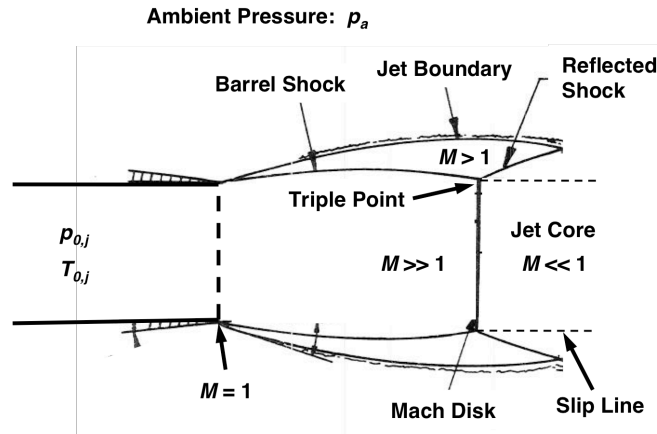


Figure 2. General structure of a highly under-expanded jet flow into a quiescent medium.^{20,21}

For supersonic retropropulsion, the highly under-expanded jet flows exhaust directly, or nearly directly, against a supersonic freestream. The aerodynamic characteristics of the body are affected by both the thrust of the jet flow and also by the interaction between the jet flow and the supersonic freestream.²³ The jet plume obstructs the oncoming freestream, and a bow shock forms. The supersonic freestream flow is decelerated to subsonic by the bow shock, and the supersonic jet flow is decelerated to subsonic by the Mach disk. A free stagnation point forms at the intersection of these two subsonic flows. A contact surface separates the subsonic jet core and the subsonic flow behind the bow shock, with a free stagnation point forming along the contact surface, as illustrated in Figure 3 for the case of a single, central jet.

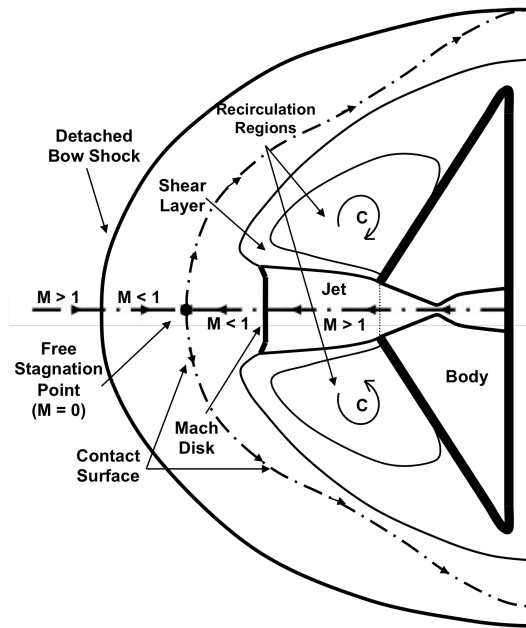


Figure 3. SRP flowfield structure for a single, central jet. (Adapted from Ref. 8)

The intersection between the freestream flow being swept aft of the body and the supersonic and subsonic flow along the shear layer forms large recirculation regions over the forebody. The shear layer is the parallel-velocity mixing region in the shock layer, between the barrel shock and the recirculation regions, and this mixing region significantly impacts the diffusion of the jet flow away from the nozzle exit. A pressure rise in the vicinity of recirculation has been observed experimentally¹¹ and tends to occur close to the jet exit on the forebody. The large velocity gradients between the subsonic flow behind the bow shock and the opposing supersonic jet flow form the supersonic shear layers that define the outer jet boundary. The recirculation and high pressure behind the bow shock force significant mixing within the shear layer surrounding the plume as the jet flow is turned. The overall effect of the jet flow – freestream interaction is the shielding of the original flow obstruction (the body) from the freestream. Experimental and analytical work have shown the jet flow to be unlikely to remain laminar through full expansion, particularly as the flow along the jet boundary reaches an annular mixing region between the Mach disk and the contact surface.²⁴ Experimental data and observation also suggest large regions of the SRP flowfield are unsteady at certain conditions⁸, with large, subsonic recirculation regions communicating disturbances and high-velocity shear layers transferring the disturbances along the jet boundary and back into the subsonic recirculation regions.

The wake aft of the body can be significantly larger than the wake for no opposing jet flow as the combination of the body and jet flow creates a larger flow obstruction than the body alone. The recirculation occurring on the forebody for bodies with supersonic retropropulsion, the freestream conditions, nozzle exit area, and thrust coefficient all potentially affect formation of the aft wake.

Flowfield stability differences between retrorpropulsion configurations have also been experimentally observed, though configuration alone does not drive the transition of the stability of the SRP flowfield.¹¹ In general, experimental work has found the flowfield stability transition conditions to be a strong function of the ratio of the exit pressure to the local ambient pressure and the ratio of the nozzle exit area to the reference area of the body⁸, both of which can be related to the shape of the contact surface formed through the aerodynamic-propulsive interaction. The flowfield can transition between two modes: a stable, blunt penetration mode and an unstable, long penetration mode. The blunt penetration mode is characterized by the penetration of the jet flow into the shock layer but not through the bow shock. The long penetration mode is characterized by the jet flow piercing the bow shock, causing a large upstream displacement of the bow shock. The transition of the flowfield is a function of the plume structure arising from the expansion condition of the jet flow. These modes are illustrated in Figure 4.

Increasing Total Pressure Ratio (or Thrust Coefficient), $P_{0,\infty} = 44.9$ psi

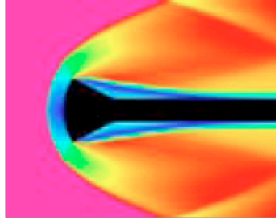


Fig. 4a Stable flowfield.

$P_{0,jet} = 0$ psi

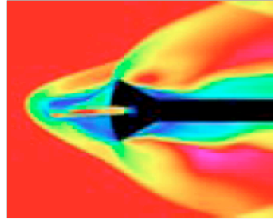


Fig. 4b Unstable flowfield.

$P_{0,jet} = 133.4$ psi

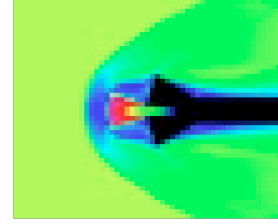


Fig. 4c Stable flowfield.

$P_{0,jet} = 590.8$ psi

Figure 4. Transition between blunt and long penetration modes.^{8,14}

Figure 5 shows the jet structures resulting from over-expanded and under-expanded conditions, as compared to the jet structure shown previously in Figure 2 for highly under-expanded conditions. In the over-expanded case ($p_1 < p_2$), the jet boundaries collapse toward the jet centerline so quickly in trying to raise the jet pressure to the local ambient pressure that subsequent reflections lack sufficient momentum within the jet flow to significantly disrupt the exterior flow. Over-expanded conditions tend to result in a blunt penetration mode. In the moderately under-expanded case ($p_1 > 3-4$ times p_2), expansion waves are reflected off of the opposing jet boundary as compression waves, or oblique shocks. Several intersecting expansion wave structures are necessary to lower the jet pressure to the local ambient pressure, creating a more oblique contact surface at an increased displacement from the body. Moderately under-expanded conditions tend to result in a long penetration mode. Highly under-expanded jet flows ($p_1 > 3-4$ times p_2) have plumes that terminate with a Mach disk and more blunt contact surfaces, as opposed to a series of intersecting expansion waves and oblique shocks and significantly more slender contact surfaces. Accordingly, highly under-expanded jet flows tend to result in a blunt penetration mode. While these transitions between blunt penetration modes and long penetration modes in flowfield stability have not been observed in the limited experimental work with peripheral configurations¹¹, transitions between the blunt and long penetration modes are expected to occur at similar pressure ratios and area ratios (i.e. expansion conditions) as observed for central configurations.

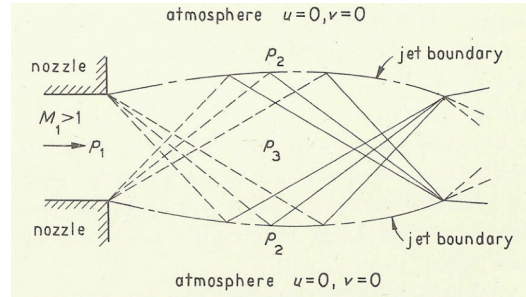
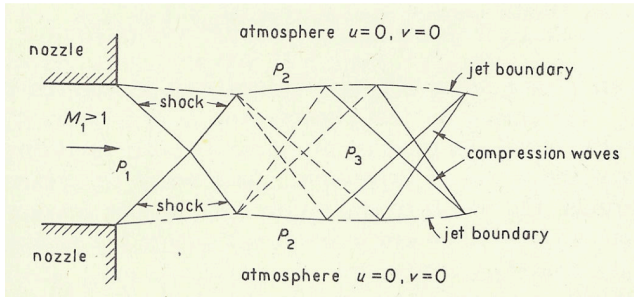


Figure 5. Jet structures for over-expanded (left) and under-expanded (right) conditions.²⁶

C. Central vs. Peripheral Supersonic Retropropulsion Flowfields

The location and configuration of retropropulsion nozzles on the vehicle forebody affects the structure of the interaction between the jet flow and the opposing freestream. Figure 3 illustrates primary flow features associated with an aerodynamic-propulsive interaction for a central retropropulsion configuration. Figure 6 illustrates similar features for a peripheral retropropulsion configuration.

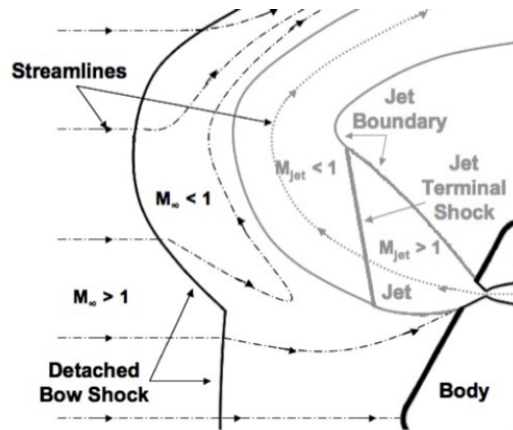


Figure 6. Flowfield characteristics for peripheral retropropulsion configurations.⁸

For the central retropropulsion configuration (Figure 3), the jet flow is directed at the center of the bow shock. The shape of the contact surface formed between the bow shock and the Mach disk is the effective shape of the flow obstruction seen by the freestream. With the impinging jet flow generally concentrated over a smaller area than the base area of the body and the Mach disk displaced upstream, the effective flow obstruction formed by the contact surface, is a more slender body than the actual body due to the displacement. This results in significantly lower surface pressures than those for the same body without a central SRP configuration.

In contrast, the jet flows in the peripheral configuration (Figure 6) are significantly less disruptive to the bow shock inboard of the nozzles, and given the less-oblique shape of the contact surface, a portion of the static aerodynamic drag can be preserved up to moderate thrust levels.¹¹ Peripheral configurations do not typically have significant flow recirculation inboard of the nozzle exits as the freestream flow is swept primarily outboard and aft of the body. As the total pressure of the jet flow increases, the individual plumes coalesce inboard into a single plume and form the flow structures characteristic of central configurations.^{11,12} The flow is highly unsteady at conditions where plume intersections are occurring, and oscillating intersections between normal and oblique shocks may generate slip lines, creating additional jet flows within the shock layer. The impingement of the jet flow on the outboard portion of the bow shock generally results in a contact surface projecting a much larger flow obstruction to the freestream flow than the body alone, resulting in a large aft wake.

D. Expected Results for Inviscid and Viscous Analysis Approaches

The relevant flow physics provide insight into the expected results of applying inviscid and viscous computational approaches to SRP flowfields. Given the significance of the recirculation and shear layer interactions on the plume structure, it is expected that inviscid approaches will be unable to fully capture the correct plume and shock structures, and accordingly, be unable to consistently capture the resultant forebody surface pressure distribution fully. However, in the vicinity of the nozzle exit, the boundary layer at the initial jet expansion is very thin, and inviscid theory has been shown to describe the resulting jet flow reasonably well.^{21,25} Further from the nozzle exit, the thickening shear layer and recirculation region have required the addition of boundary layer approximations to inviscid theory to capture the jet structure fully.²¹

The presence of supersonic free shear layers within SRP flowfields suggests viscous dissipation of both the jet and freestream momentum to play an important role in the formation of the flow structure away from the nozzle exit. Work²⁷ has been completed on the transition from laminar to turbulent flow along free supersonic shear layers and on differences in transition behavior between subsonic and supersonic free and wall-bounded shear layers. However, much of this work is experimental and/or analytical, and current models in use may not reflect such behaviors. However, experimental observation of flow transition for jets exhausting into quiescent mediums and supersonic cross flows^{20,22} and the formation of large mixing regions in SRP flowfields suggest a strong potential for transition. Appropriate turbulence modeling is still likely to be a significant contributor to the ability to consistently capture the true flow structure and resulting pressure distribution.

The complexity of the SRP flowfield, with subsonic recirculation and supersonic and subsonic shear layers, does not allow for an a priori expectation that the flowfield will be steady, though experimental observation and data

suggest that the flowfield may under certain conditions be unsteady. The degree to which viscous dissipation lessens the potential for unsteadiness is unclear, but flow solutions obtained using viscous approaches are expected to be more steady than otherwise equivalent inviscid analysis techniques. Similarly, viscous – turbulent approaches are expected to be steadier than otherwise equivalent viscous – laminar approaches due to the addition of turbulent dissipation. The effectiveness of all of these flow solution approaches will be highly dependent on the specific models applied and how certain models, e.g. turbulence and turbulent transition, are coupled to the flow solver.

Independent of the analysis approach, computational solutions for SRP flowfields will be computationally expensive. The complexity of the interaction between the jet flow and opposing freestream and between the resulting flow structures will require a high degree of grid resolution over a large volume. Additionally, the increased size of the freestream flow disturbance caused by the jet flow will require a much larger computational domain, particularly the downstream outflow boundary distance, than for the same blunt body with no supersonic jet flow. If steady-state solutions are unable to capture critical flow behavior, the computational cost will increase further for conditions requiring time accurate solutions.

III. Approach and Models

The general approach is to generate flow solutions for two extremes in retropropulsion configuration at conditions that span available experimental data and extend toward flight-relevant operation. FUN3D is used for inviscid, viscous – laminar, and viscous – turbulent analyses, with all cases run to a steady-state solution. Steady-state solutions are obtained with FUN3D using local time stepping to drive a 2nd order accurate spatial residual to steady-state. Steady-state convergence is determined here through a three order of magnitude drop in the x-momentum residual and maintenance of this drop through several hundred additional iterations. With an objective of this work being to understand the change in static aerodynamic trends with thrust coefficient for two SRP configurations, $p_{0,j}$ is the only parameter varied between cases. For consistency with the experimental data, the freestream is fixed at $M_\infty = 2.0$, and all cases assume air for the composition of both the freestream and the jet flow.

A. Computational Tool – FUN3D

FUN3D is a fully unstructured, NASA-developed CFD code capable of solving the Euler and Reynolds-averaged Navier-Stokes (RANS) equations through both perfect gas and thermochemical equilibrium/non-equilibrium simulation.²⁸⁻³⁰ The flow solver is based on second-order, node-centered, finite volume discretization. Local time stepping is applied for steady flows, and 2nd order time accuracy is applied for unsteady flows. The scheme utilizes implicit upwind-differencing and, similar to recent work by Trumble, et al.⁹, Edwards' dissipative LDFSS flux function³¹ with a Van Albada limiter.³² The RANS flow solver is coupled to Menter's SST turbulence model³³, with no compressibility correction. FUN3D was selected as the flow solver in this investigation as a result of its common application to entry vehicle aerodynamics and various nozzle and jet flow cases.²⁸ All solutions have been generated using version 10.8 of the FUN3D code.

The solutions are generated using the same unstructured, tetrahedral grid for each configuration. The grids are of medium resolution and constructed with linear sources in the regions of jet flow expansion and freestream shock locations. Continuing work beyond this investigation includes grid resolution studies. The computational domains are large, with the inflow boundary 10D upstream of the body and the outflow boundary 15-20D downstream of the body.

B. Experimental Data Set and Conditions Summary

The experimental data set used in this investigation is from a wind tunnel test series completed by Jarvinen and Adams¹¹ from 1968 – 1970. This work is the only published data for a parametric test series spanning both central and peripheral retropropulsion configurations.⁸ The test series was conducted in the NASA Ames 6 ft. x 6 ft. supersonic wind tunnel across freestream Mach numbers of 0.4 to 2.0. In total, the test series explored the effects of aeroshell geometry (45° and 60° sphere-cones), retropropulsion configuration (one central nozzle vs. three peripheral nozzles), exhaust gas composition (air and helium), angle of attack (+9° to -18°), thrust coefficient (0 to 7, at supersonic freestream conditions), and differential throttling in air.¹¹ Of interest in this investigation are the data for the 60° sphere-cone at $M_\infty = 2.0$ and $\alpha = 0^\circ$, for all C_T tested with air as the exhaust gas.

The experimental data set includes surface pressure distributions, integrated force and moment coefficients, and flowfield geometry information as a function of thrust coefficient. The 4-inch diameter models were instrumented

with concentric rings of pressure taps on the forebody: 30 taps on the single nozzle model and 45 taps on the three-nozzle model. Force and moment data were generated by integrating these pressure measurements over the model.¹¹ All cases were run with $p_{0,\infty} = 2$ psia (13.79 kPa), changing C_T by varying the jet total pressure. The experimental data set¹¹ does not provide information on the freestream total temperature or the plenum total temperature. In this investigation, $T_{0,j}$ was assumed to be 294 K to be consistent with other SRP investigations completed in the 1960s using compressed, dry air. $T_{0,\infty}$ was assumed to be 311.67 K to be consistent with the operating envelope of the NASA Ames 6 ft. x 6 ft. supersonic tunnel.³⁴ In addition to an absence of total temperature information, the experimental data set does not provide information on data collection or reduction methods, resulting in only an approximate knowledge of the test conditions. Though not reported in the original experiment, the model geometry and test conditions likely yielded very low temperatures in the jet plumes and the possibility of liquefaction. Complimentary work¹² with the experimental data set from Jarvinen and Adams has observed single-digit Kelvin temperatures in the jet plume with the assumption of no phase change in the jet flow and the same test conditions as those used in this investigation. No special treatment is applied here concerning the potential of phase change in the jet flow.

All run conditions are determined assuming 1-D isentropic flow through the nozzle, with stagnation conditions defined for the nozzle plenum. Conditions at the plenum face are used in place of stagnation conditions as inputs to FUN3D. Table 1 provides a summary of the plenum pressure and thrust coefficient for the cases run. A C_T of zero does not correspond to a plenum pressure of zero; the plenum velocity is non-zero. Additionally, a minimal plenum pressure is required to prevent opposing freestream flow from expanding into the plenum. Table 2 provides a summary of the conditions common to all cases. Only the $C_T = 7.00$ conditions are considered to be flight-relevant for Mars exploration missions. Experimental data at flight-relevant conditions ($C_T > 5$) is extremely limited in the existing SRP knowledge base.

Table 1. Run Summary

Central Retropropulsion Configuration			Peripheral Retropropulsion Configuration		
Run	$p_{0,j}$ (psi)	C_T	Run	$p_{0,j}$ (psi), per nozzle	$C_{T,total}$
1	2.140	0.00	1	1.153	0.00
2	767.9	2.00	2	638.2	1.66
3	1549.0	4.04	3	1553.1	4.04
4	2682.3	7.00	4	2691.0	7.00

Table 2. Common Run Conditions

Parameter	Value
M_∞	2.0
$\gamma_\infty = \gamma_j$	1.4
$p_{0,\infty}$	2.0 psi
p_∞	0.256 psi
$T_{0,\infty}$	311.7 K
T_∞	172.4 K
$T_{0,j}$	294.0 K
α	0°

C. Configurations

Two retropropulsion configurations are considered: a central retropropulsion configuration with a single nozzle and a peripheral retropropulsion configuration with three nozzles. Both configurations have conical nozzles with exit planes that are flush with the aeroshell forebody. The aeroshell is a 4-inch diameter, 60° sphere-cone forebody with a flat aft section. Both configurations are consistent with those tested by Jarvinen and Adams.¹¹

1. Central Retropropulsion Configuration (Single Nozzle)

The central retropropulsion configuration has a single nozzle aligned with the body axis of symmetry. Figure 7 shows the geometry of the aeroshell model, and Figure 8 shows the dimensions of the nozzle and plenum. The nozzle is a 15° conical nozzle with a 0.5-inch exit diameter. The nozzle has an area ratio, A_e/A^* , of 13.95, corresponding to an exit Mach number of 4.3, assuming 1-D isentropic expansion. A sting (length: 4-inch, diameter: 1-inch) has been added to the aft face of the original model.

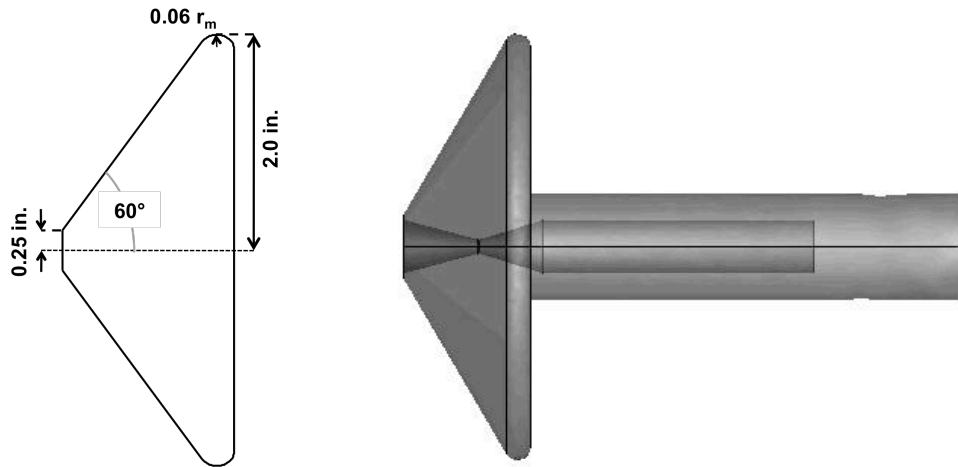


Figure 7. Aeroshell geometry¹¹ and nozzle location.

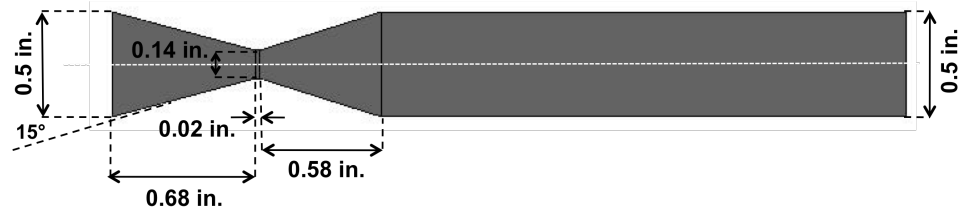


Figure 8. Nozzle dimensions for the central retropropulsion configuration.

2. Peripheral Retropropulsion Configuration (Three Nozzles)

The peripheral retropropulsion configuration has three nozzles, spaced 120° apart on a circle at $0.8 r_m$. The nozzles are 15° conical nozzles, each scarfed at 30° to be flush with the model forebody. Figure 9 and Figure 10 show the location of the nozzles on the aeroshell forebody and the nozzle dimensions. The three nozzles were designed to collectively have the same performance as the single, central nozzle for the same total thrust coefficient. In the original experiment, the model did not have an aft section; all plumbing behind the forebody was exposed. A 1-inch long cylindrical aft section has been added past the shoulder in this investigation to simplify the flowfield aft of the model.

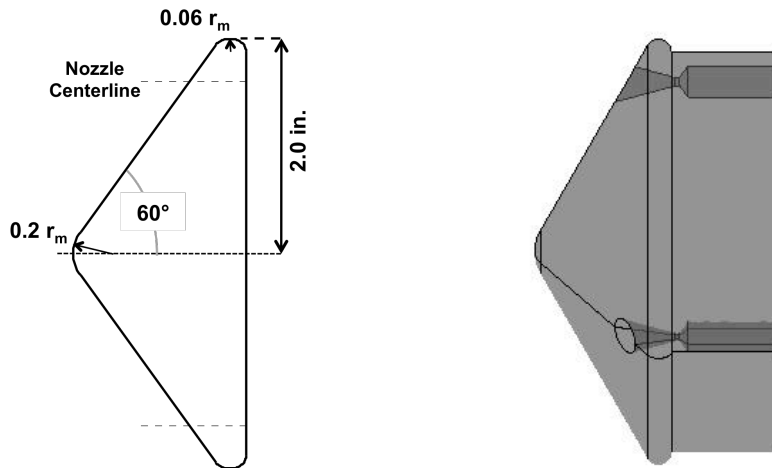


Figure 9. Aeroshell geometry¹¹ and nozzle locations.

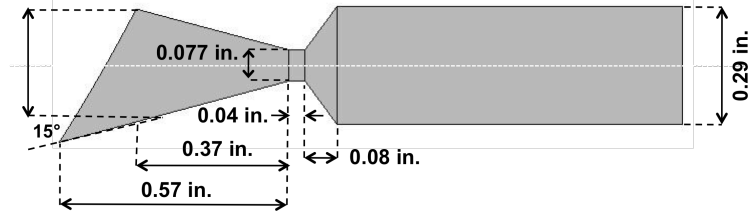


Figure 10. Nozzle dimensions for the peripheral retropropulsion configuration.

IV. Preliminary Results

For both the central and peripheral retropropulsion configuration, solutions have been generated for each case listed in Table 1 using a steady-state, viscous – turbulent approach. To illustrate the effects of the computational addition of viscosity, an inviscid and a viscous – laminar approach have been applied to both retropropulsion configurations for the $C_T = 4.04$ condition. Mach contours are shown to illustrate the SRP flowfield structure, and streamlines are generated to highlight critical flow features. Distributions of C_p as a function of radial distance on the forebody are also given for three angular locations for each set of conditions. No integrated force coefficients are given, as the coefficients given in the experimental data set were originally integrated from a limited number of surface pressure measurements, and no information regarding the uncertainty in these measurements is given in the test report.¹¹

A. Central Configuration

As discussed in Section II.B, the central configuration should provide a symmetric jet structure defined along a constant pressure boundary and a terminal Mach disk. A free stagnation point should form on the contact surface along the body axis in the subsonic region between the bow shock and the Mach disk. The axial locations of the Mach disk, stagnation point, and bow shock for the viscous – turbulent solutions and experimental data are given in Figure 11. All axial locations show good agreement with the experimental data, indicating that the computational solutions likely captured the flow interaction along the body centerline. The stagnation point location and bow shock location imply that the contact surface near the axis of symmetry is being determined reasonably well in comparison with the experimental data, as the contact surface defines the location of the free stagnation point as well as the effective flow obstruction seen by the freestream.

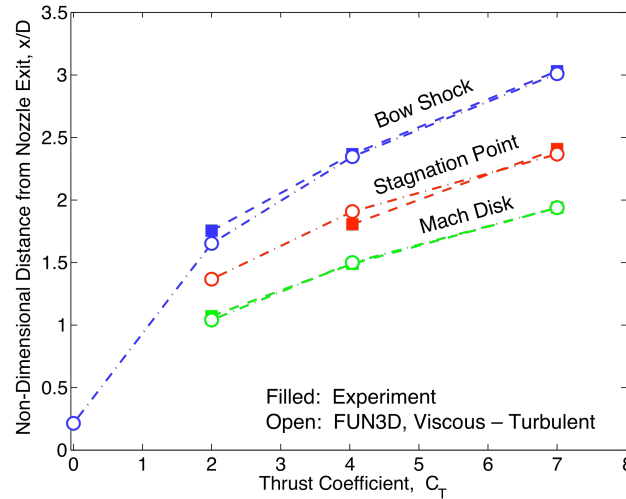


Figure 11. Non-dimensional axial location of flow structures with increasing C_T .

Mach contours for the central configuration cases are shown in Figure 12 for each C_T . The solution with no jet flow shows the bow shock located near the body as expected. Flow separation occurs around the shoulder, creating a wake region aft of the vehicle. As C_T increases, the subsonic wake region expands further aft of the vehicle, indicating that the area of the effective freestream flow obstruction is increasing with C_T . The Mach disk is clearly visible at each condition in Figure 12, and the increase in the area of the effective freestream flow obstruction can be attributed to the progressive increase in the area of the Mach disk with C_T . The triple point is visible at the location

of the intersection between the Mach disk and the barrel shock and represents the structures required to turn the flow. These flow features are marked on Mach contours in Figure 13. The barrel shock is defined in the Mach contours as a thin supersonic region along the edge of the supersonic jet flow. The shear layer also exists in this region, as seen in the Mach contours as well as the streamlines showing the flow path along the outer boundary of the barrel shock, where supersonic jet flow is mixing with parallel subsonic recirculation flow. Streamlines also indicate the location of the contact surface and free stagnation point between the bow shock and Mach disk. After passing through the bow shock, the freestream streamlines are turned to run parallel to the turning streamlines of the jet flow. This interface where the streamlines intersect is the contact surface, apparent in Figure 12. The free stagnation point exists where the streamlines change the direction in which they pass around the contact surface and is located along the body axis. The recirculation regions between the supersonic jet flow boundary and the freestream flow being swept aft of the body are also apparent from the streamlines in Figure 12 for $C_T = 7.00$ conditions.

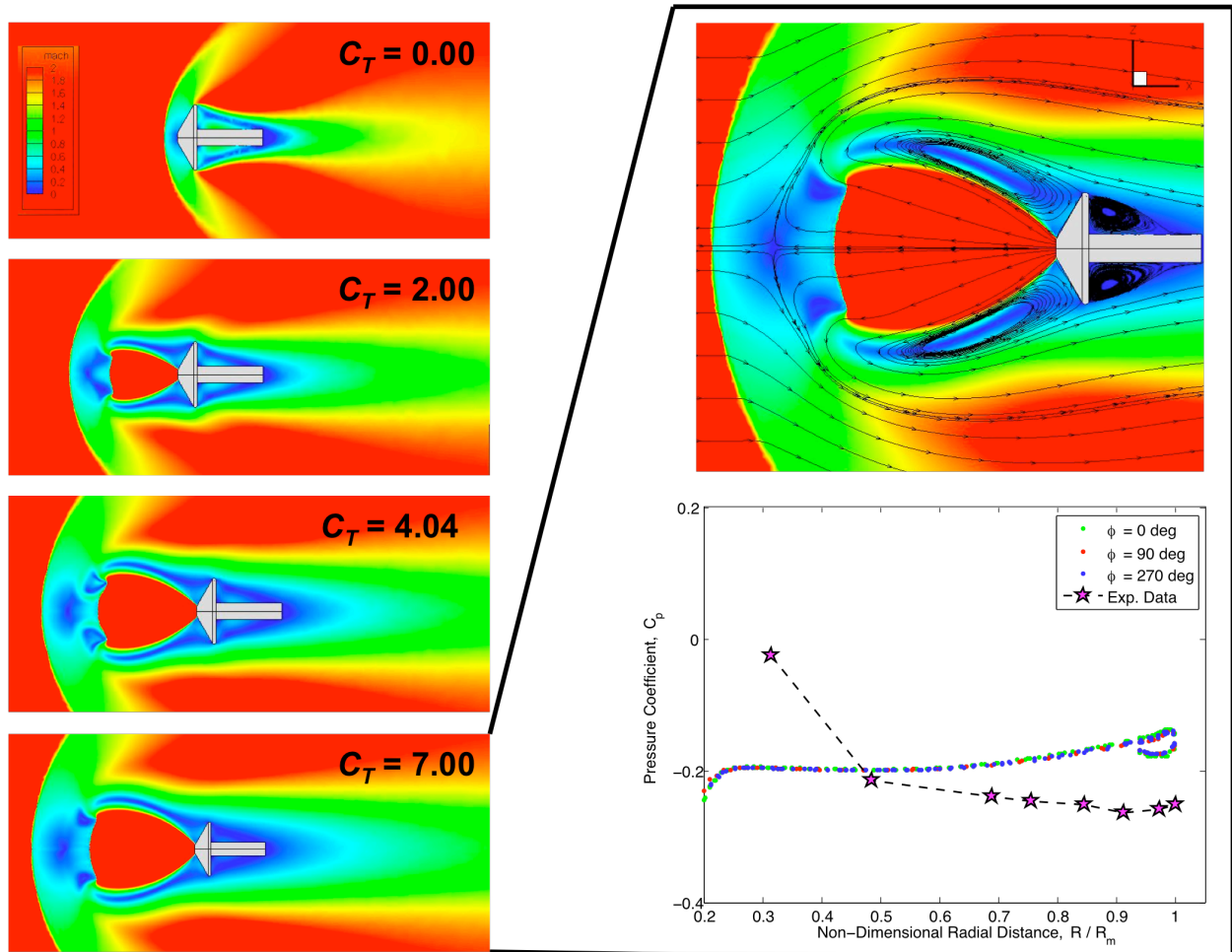


Figure 12. Mach contours for the central configuration. Streamlines and radial C_p distribution for $C_T = 7.00$.

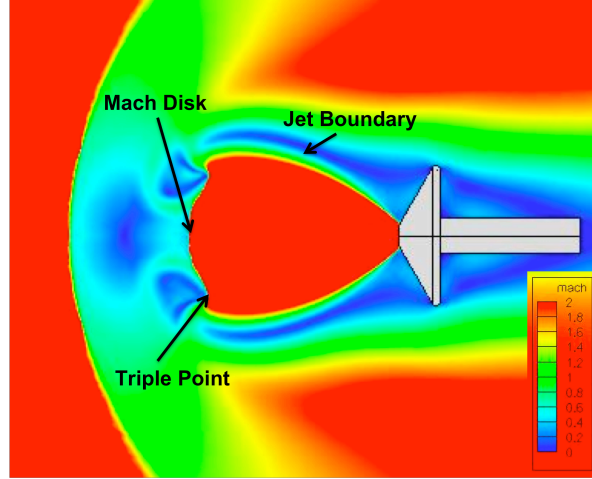


Figure 13. Mach contours and location of primary flow features ($C_T = 4.04$).

The experimental results show a negligible change in pressure near the shoulder for all cases with the jets active, while the CFD solutions show a larger rise in surface pressure in this region, as shown in Figure 14. The pressure rise at the shoulder is not necessarily caused by re-attachment of the flow, as re-attachment was not observed at every condition. While there is no information available on the uncertainty of the pressure measurements in the experimental data, particularly at the low pressures observed, the maintenance of the reduction in surface pressure towards the shoulder is consistent with similar test series.⁸ In addition, the expansion of the jet plume at the nozzle exit affects the pressure distribution in the region near the nozzle exit. The experimental data shows a significant rise in C_p near the nozzle exit, while the CFD solution shows a relatively constant C_p value across the forebody in this region for each C_T value. This appears to indicate that the CFD solution may not be capturing the proper expansion angle at the nozzle exit. No data is provided from the experiment with regard to the jet structure near the vehicle to verify that this is the cause of the difference in surface pressure.

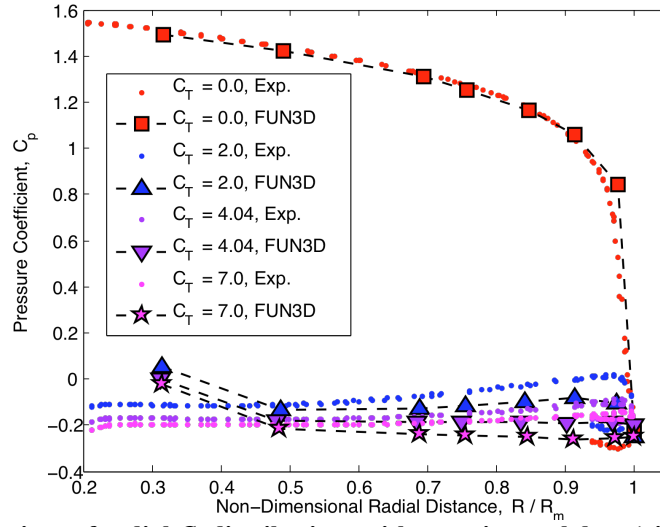


Figure 14. Comparison of radial C_p distributions with experimental data (viscous – turbulent).

The viscous – turbulent solutions all converged to a steady-state condition with a plume geometry agreeing reasonably well with the measured locations in the experimental data and qualitatively with the theoretical flow physics. For a preliminary comparison to the viscous – turbulent approach applied to the solutions given in Section IV.A, the $C_T = 4.04$ case was run using both an inviscid and a viscous – laminar approach. The initial Mach contours for these approaches are shown in Figure 15. Both the inviscid and viscous – laminar solutions exhibit asymmetric flows, and the residual histories indicate likely unsteady behavior within the flow solution. In particular, the jet boundary for both cases shows a much different structure from the viscous – turbulent solution.

The triple point is more sharply defined, as the reflected shocks form a different shape. The jet boundary does not tend back towards the centerline as much as is seen in the viscous – turbulent solution, forming the triple point and reflected shock structure differently. The rapidly expanding shear layers along the jet flow likely result in an increased influence of viscosity as the jet expands away from the nozzle exit, possibly contributing to the deviation in plume structure observed in solutions obtained using an inviscid approach. Without extensive shear layer formation, an inviscid approach should do reasonably well in predicting the plume structure, assuming losses along the nozzle walls are negligible.²⁵

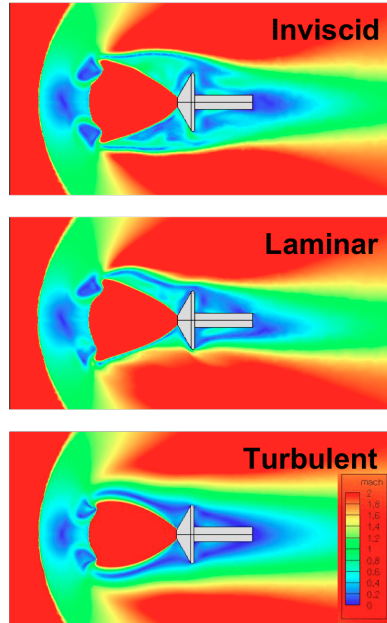


Figure 15. Mach contours for the central configuration at $C_T = 4.04$, comparing analysis approaches.

The asymmetry in the jet structure is apparent in both the recirculation over the forebody and in the wake flow aft of the body, visible in the Mach contours in Figure 15. The wake flow is asymmetric for the inviscid and viscous – laminar cases as a result of the variation in the jet structure and associated shape of the contact surface. Locally, as the effective flow obstruction shape varies, the decelerated freestream flow will behave differently as a function of angular location, resulting in asymmetry over the forebody and in the wake. The viscous – laminar solution shows better symmetry than the inviscid solution, possibly indicating the steadying or damping effect of viscous dissipation on the flowfield. The viscous – turbulent approach is the only approach for which converged, steady-state solutions were obtained. Both the inviscid and viscous – laminar cases will need to be explored further using a time accurate approach.

B. Peripheral Configuration

For the peripheral configuration, the jet flows form a significantly different flowfield structure as compared to the central configuration, while the individual jet plume structures remain similar. The jet flows develop a shear layer along the jet boundary, and a Mach disk forms to terminate the supersonic jet flow for highly under-expanded conditions. The nozzle geometry for the peripheral configuration is such that the total C_T for the three nozzles in the peripheral configuration is equal to the C_T for the single nozzle in the central configuration. As compared to the central configuration, the peripheral configuration requires a higher total C_T to be at highly under-expanded conditions, delaying the formation of the Mach disk to higher C_T 's. The subsonic region inboard of the jet plumes in the peripheral configuration does not contain recirculation and retains a higher pressure than the surface pressure for the central configuration at the same conditions.

The preliminary solutions for the viscous – turbulent approach are shown in Figure 16 for the four C_T 's listed in Table 1. Mach contours are shown, scaled to Mach 3 to highlight different flow features. The Mach contours are for two transparent, planar slices to show the 3-dimensional flowfield structure. Each slice passes through the center of a nozzle, making two jet plumes visible in this orientation. The forebody C_p distributions are also shown for

each C_T . Analogous to Figure 13, Figure 17 points out the Mach disk, triple point, and jet boundary for the peripheral configuration on Mach contours for $C_T = 7.00$ conditions.

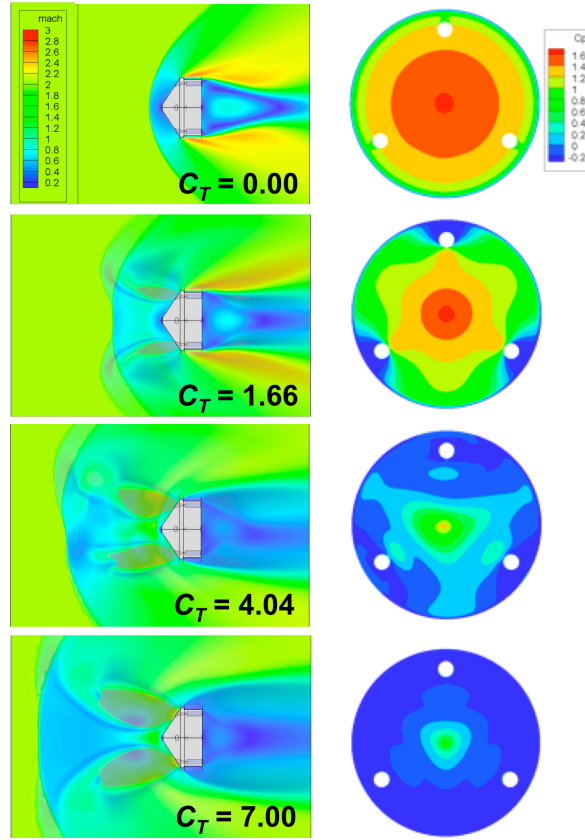


Figure 16. Mach contours and C_p contours for the peripheral configuration with varying C_T .

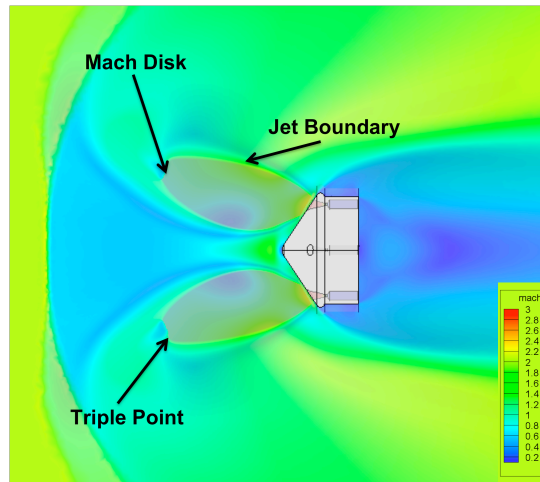


Figure 17. Mach contours and locations of primary flow features ($C_T = 7.00$).

For the $C_T = 0.00$ case, the flowfield structure agrees with the similar solution for the central configuration. The difference in geometry between the two configurations is the spherical nose cap on the peripheral configuration, which results in a slightly different pressure distribution near the body axis as compared to the central configuration, which has the nozzle exit plane open to the freestream. Each case with jet flow exhibits a different plume structure and, subsequently, a different contact surface is formed. The $C_T = 1.66$ case presents a weakly under-expanded jet

and exhibited steady behavior in the solution residual history. As shown in the Mach contours in Figure 16, the jet plumes are symmetric, resulting in a symmetric pressure distribution. The pressures inboard of the nozzles remains near the pressures seen for the $C_T = 0.00$ case, indicating that surface pressure, and accordingly, the static aerodynamic drag is being preserved inboard of the nozzles at $C_T = 1.66$. However, as shown in Figure 18, the pressure distribution is not in agreement with the experimental C_p distribution at these conditions. Along circles of constant radius, C_p at radii near that of the nozzles shows a noticeable variation in the experimental data, depending on proximity to the nozzle exits. The general shape for these radii is in agreement, but the CFD solution consistently shows a higher pressure than the experimental data at all angular locations. At radii inboard of the nozzles, the pressure should be more constant with variation in angular location, which is consistent between the CFD solution and the experimental data. Again, the actual value of C_p in this region is higher for the CFD solution. Since preservation of the forebody surface pressure decreases with increasing C_T , and the jet expansion from the nozzle increases with increasing C_T , it is thought that the CFD solution is under-predicting the jet expansion in the immediate inboard vicinity of the nozzle exit. If the CFD were to predict a larger jet expansion for this thrust condition, then the pressure values along the forebody would drop and agree more closely with the experimental results.

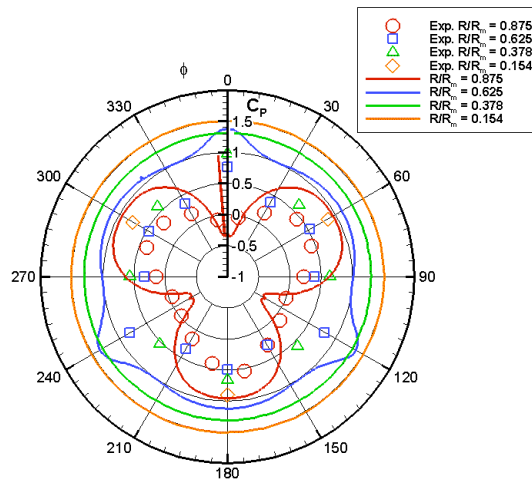


Figure 18. Comparison of the circumferential C_p distribution for $C_T = 1.66$ with experimental data.

The conditions corresponding to a C_T of 4.04 yielded an asymmetric flowfield structure as the degree of under-expansion of the jet flow increased as compared to the cases with lower thrust coefficients. In the Mach contours shown in Figure 16, a secondary plume cell is visible after the jet flow passes through the terminal shock structure (conditions do not yet correspond to those for the formation of a Mach disk). The C_p distribution is also asymmetric, a result of the pressure around each nozzle varying with respect to each other. Both the residual history and flowfield and C_p distribution asymmetry suggest the flowfield behavior to be unsteady at $C_T = 4.04$ conditions. Even with the unsteadiness in the flow solution, the pressure inboard of the nozzles is not preserved to the same degree as seen for the lower C_T conditions. As the jet flows expand inward, less pressure is preserved on the forebody. This case will likely need to be simulated using a time accurate approach.

For the $C_T = 7.00$ case, the solution is exhibiting steady behavior similar to that observed for the $C_T = 1.66$ case. Each jet flow more clearly resembles the expected flow structure, shown previously in Figure 6. Figure 16 shows a significant improvement in the symmetry between the two visible plumes than the $C_T = 4.04$ case. The jet boundaries have expanded further inboard of the nozzles than is seen for either of the lower thrust coefficient conditions, further decreasing the forebody pressure near the body axis. However, the degree of pressure preservation is still greater than that expected from the experimental data, as shown in Figure 19. This was similarly seen in the $C_T = 1.66$ case, where the CFD solution is not accurately capturing the jet expansion and preserving higher pressures along the forebody than those given in the experimental data. The streamlines for $C_T = 7.00$, also shown in Figure 19, are qualitatively in agreement with the expected flowfield for a peripheral configuration. The flow inboard of the nozzles is not contained within a recirculation region, but instead is turned towards the jet flow and then aft of the body and away from the other plumes. The contact surface that forms between the decelerated freestream flow and the subsonic jet flow extends outboard of the true body diameter. The larger effective

obstruction to the freestream results in a larger wake region aft of the body than has been observed for the central configuration.

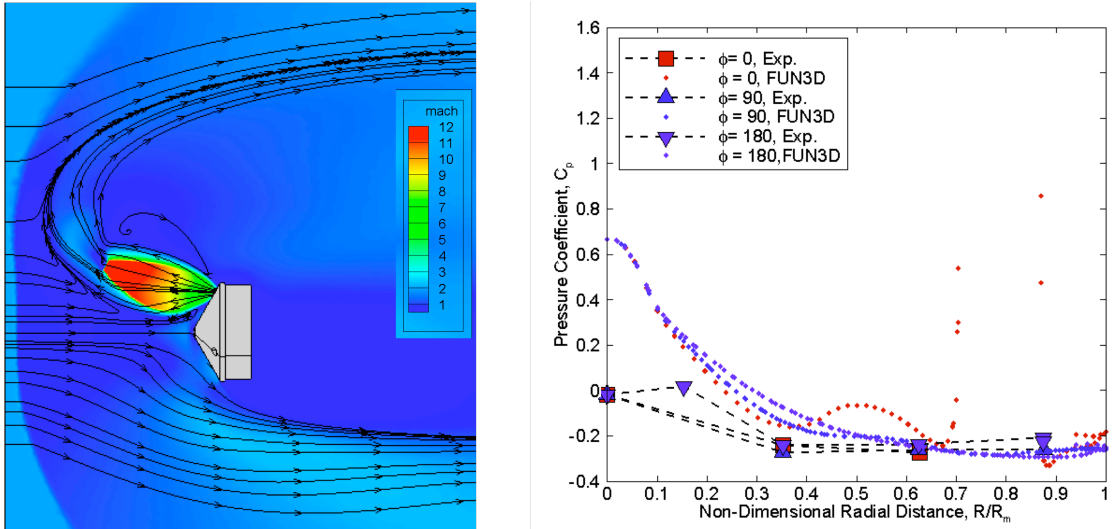


Figure 19. Streamlines and radial C_p distributions for the peripheral configuration with $C_T = 7.00$.

As with the central configuration, one peripheral configuration case has been run with inviscid and viscous – laminar approaches in addition to the viscous – turbulent approach. Despite the apparent unsteadiness of the viscous – turbulent solution, the same conditions ($C_T = 4.04$) are used, as this total thrust coefficient is equivalent to the conditions run for the central configuration using the same approaches. It is expected that the inviscid and viscous – laminar approaches will also exhibit unsteady behavior at these conditions. The Mach contours and C_p distributions for the inviscid, viscous – laminar, and viscous – turbulent approaches are shown in Figure 20.

In the inviscid solution, the jet plumes have clearly defined terminal shocks. However, the residual histories and Mach contours suggest a high degree of unsteadiness. The jet plumes themselves are roughly symmetric, but the turned jet flow is not symmetric. The wake region is highly asymmetric, likely due to the changing shape of the contact surface. The pressure on the forebody also shows asymmetry, as seen in the viscous – turbulent solution. The C_p distribution is not symmetric around each nozzle, and the preservation of the pressure inboard of the nozzles is higher than that seen for the viscous – turbulent case.

For the viscous – laminar approach, the flowfield shows less unsteadiness than the inviscid solution. The flowfield still exhibits unsteady behavior in the residual histories and flowfield asymmetries in the wake region and outboard of the jet plumes. The pressure inboard of the nozzles is reduced further than in the inviscid case, but the pressure has not been reduced as much as in the viscous – turbulent case. Since the viscous – laminar jet plumes have more inboard expansion than the inviscid approach, but not as much as the viscous – turbulent case, this is in agreement with the expected flow structure. Due to the inclusion of both viscous and turbulent dissipation, the viscous – turbulent solution exhibits the least unsteady behavior of the three approaches.

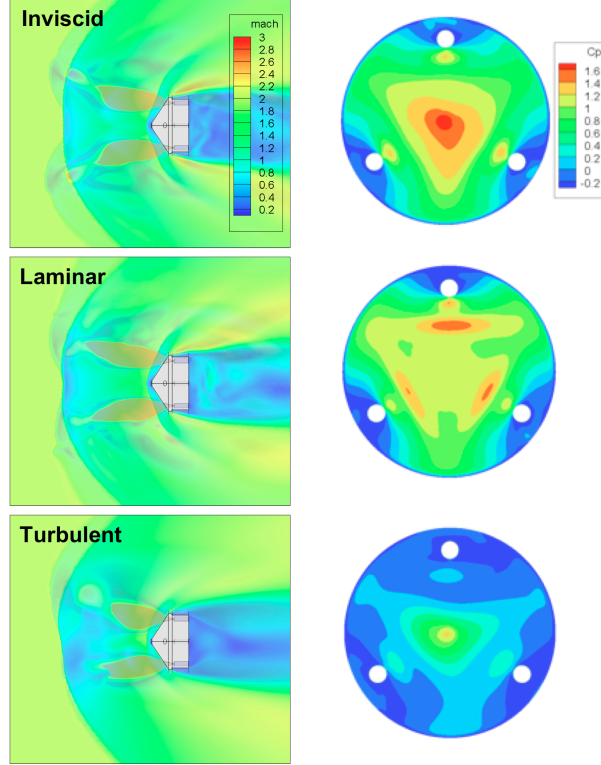


Figure 20. Mach contours and C_p contours for the peripheral configuration at $C_T = 4.04$.

V. Concluding Remarks

Supersonic retropropulsion is an enabling decelerator technology for high-mass planetary entries at Mars. SRP flowfields are the result of a complex interaction between typically highly under-expanded jets and a directly, or nearly directly, opposing supersonic freestream. The jet flows are characterized by a constant pressure jet boundary, shear layers along the jet boundaries, and a terminal shock structure. In the case of highly under-expanded jet flows, the terminal shock structure for the jet is a Mach disk. The interaction between the shear layer and the jet flow forms a contact surface between the bow shock and the jet flow. The shape of this contact surface is the effective flow obstruction seen by the freestream, and the resulting change in surface pressure distributions significantly alters the static aerodynamic characteristics of the body as compared to the same body with no SRP.

Accurate and consistent simulation of SRP flowfields is of significant interest to the NASA technology development community. A lack of modern experimental data at relevant conditions and incomplete existing data challenge efforts to validate existing computational tools and approaches. This investigation presented a discussion of the relevant flow physics to provide insight into the effectiveness of inviscid and viscous computational analysis approaches in consistently and accurately capturing the relevant flow physics. Preliminary computational results for a blunt body with two retropropulsion configurations were compared with experimental data for the location of prominent flow features and surface pressure distributions. This work was intended to provide an initial discussion of the challenges facing the computational simulation of supersonic retropropulsion flowfields.

The viscous – turbulent analysis approach employed here agrees reasonably well with experimental data for the axial locations of the bow shock, free stagnation point, and Mach disk and converged to steady-state for a central retropropulsion configuration. However, the surface pressure distributions agree less well, showing a pressure rise towards the shoulder that has not been observed in experiment. The flowfield structures for a peripheral retropropulsion configuration agree qualitatively with the expected structures, but proper inboard jet flow expansion is not being captured, and accordingly, pressure is preserved inboard of the nozzles to higher thrust coefficients than has been observed in experiment. A number of the cases considered here exhibit unsteady behavior and will likely require time accurate simulation to complete their assessment.

Inviscid and laminar approaches are more likely to be unsteady than turbulent approaches, and such behavior is suggested in the preliminary results presented here. In the thickening shear layers and recirculation region away from the nozzle exit affect the dissipation of the jet flow and in regions away from the nozzle exit, viscous approaches are likely required to accurately capture the jet structure and subsonic interaction regions. It is unclear when or where the jet flow may transition from laminar to turbulent, though preliminary computational solutions using viscous – turbulent approaches have tended to agree better with experimental results than viscous – laminar approaches, though Menter’s SST turbulence model may provide too much dissipation in the flowfield. The apparent unsteadiness of the inviscid and viscous – laminar solutions at certain conditions will require time accurate simulation to be directly compared with the equivalent viscous – turbulent approach. Gridding approaches and convergence, though not addressed here, will also require treatment in future work.

Acknowledgments

The authors thank the following individuals for their assistance and support of this work: Bil Kleb (NASA LaRC), Artem Dyakonov (NASA LaRC), Michael Park (NASA LaRC), Dana Hammond (NASA LaRC), Ian Clark (JPL), Michael Aftosmis (NASA ARC), and Noel Bahktian (Stanford University). The authors also acknowledge the support of this work by the NASA Fundamental Aeronautics Program Hypersonics Project and the NASA Exploration Technology Development Program Supersonic Retropropulsion team.

References

- ¹Braun, R. D., and Manning, R. M., “Mars Exploration Entry, Descent, and Landing Challenges,” *Journal of Spacecraft and Rockets*, Vol. 44, No. 2, 2007, pp. 310–323.
- ²Steinfeldt, B. A., Theisinger, J. E., Korzun, A. M., Clark, I. G., Grant, M. J., and Braun, R. D., “High Mass Mars Entry, Descent, and Landing Architecture Assessment,” AIAA Paper 2009-6684, Sept. 2009.
- ³Price, H., Hawkins, A. M., and Radcliffe, T. O., “Austere Human Missions to Mars,” AIAA Paper 2009-6685, Sept. 2009.
- ⁴Drake, B. G., ed., “Human Exploration of Mars: Design Reference Architecture 5.0,” NASA-SP-2009-566, July 2009.
- ⁵Marsh, C. L., and Braun, R. D., “Fully-Propulsive Mars Atmospheric Transit Strategies for High-Mass Payload Missions,” IEEEAC Paper 1219, Mar. 2009.
- ⁶Christian, J. A., Wells, G. W., Lafleur, J. M., Verges, A. M. and Braun, R. D., “Extension of Traditional Entry, Descent, and Landing Technologies for Human Mars Exploration,” *Journal of Spacecraft and Rockets*, Vol. 45, No. 1, 2008, pp. 130–141.
- ⁷Zang, T. A., and Tahmasebi, F., “Entry, Descent and Landing Systems Analysis (EDL-SA) for High Mass Exploration and Science Mars Mission Systems: Year 1 Report,” NASA EDLSA-002, Nov. 2009.
- ⁸Korzun, A. M., Braun, R. D., and Cruz, J. R., “Survey of Supersonic Retropropulsion Technology for Mars Entry, Descent, and Landing,” *Journal of Spacecraft and Rockets*, Vol. 46, No. 5, 2009, pp. 929–937.
- ⁹Korzun, A. M., and Braun, R. D., “Performance Characterization of Supersonic Retropropulsion for Application to High-Mass Mars Entry, Descent, and Landing,” AIAA Paper 2009-5613, Aug. 2009.
- ¹⁰Edquist, K. T., Dyakonov, A. A., Shidner, J. D., Studak, J. W., Tigges, M. A., Kipp, D. M., Prakash, R., Trumble, K. A., Dupzyk, I. C., and Korzun, A. M., “Development of Supersonic Retro-Propulsion for Future Mars Entry, Descent, and Landing Systems,” AIAA 2010-5046, June 2010.
- ¹¹Jarvinen, P. O., and Adams, R. H., “The Aerodynamic Characteristics of Large Angled Cones with Retrorockets,” NASA CR NAS 7-576, Feb. 1970.
- ¹²Trumble, K. A., Schauerhamer, D. G., Kleb, W. L., Carlson, J.-R., Buning, P. G., Edquist, K. T., and Barnhardt, M. D., “An Initial Assessment of Navier-Stokes Codes Applied to Supersonic Retro-Propulsion,” AIAA 2010-5047, June 2010.
- ¹³Bakhtian, N. M., and Aftosmis, M. J., “Parametric Study of Peripheral Nozzle Configurations for Supersonic Retropropulsion,” AIAA 2010-1238, Jan. 2010.
- ¹⁴Daso, E. O., Prichett, V. E., and Wang, T-S, “The Dynamics of Shock Dispersion and Interactions in Supersonic Freestreams with Counterflowing Jets,” AIAA Paper 2007-1423, Jan. 2007.
- ¹⁵Hayashi, K., Aso, S., and Tani, Y., “Numerical Study of Thermal Protection System by Opposing Jet,” AIAA Paper 2005-0188, Jan. 2005.
- ¹⁶Hayashi, K., and Aso, S., “Effect of Pressure Ratio on Aerodynamic Heating Reduction due to Opposing Jet,” AIAA Paper 2003-4041, June 2003.
- ¹⁷Cheng, G. C., Neroorkar, K. D., Chen, Y-S, Wang, T-S, and Daso, E. O., “Numerical Study of Flow Augmented Thermal Management for Entry and Re-Entry Environments,” AIAA Paper 2007-4560, June 2007.
- ¹⁸Chang, C-L, Venkatachari, B. S., and Cheng, G. C., “Effect of Counterflow Jet on a Supersonic Reentry Capsule,” AIAA Paper 2006-4776, July 2006.
- ¹⁹Gnoffo, P. A., “Planetary-Entry Gas Dynamics,” *Annual Review of Fluid Mechanics*, Vol. 31, 1999, pp. 459–494.
- ²⁰Wilkes, J. A., Glass, C. E., Danehy, P. M., and Nowak, R. J., “Fluorescence Imaging of Underexpanded Jets and Comparison with CFD,” AIAA 2006-910, Jan. 2006.
- ²¹Pindzola, M., “Jet Simulation in Ground Test Facilities,” AGARDograph No. 79, Nov. 1963.

- ²² Viti, V, Neel, R., and Schetz, J. A., “Detailed Flow Physics of the Supersonic Jet Interaction Flow Field,” *Physics of Fluids*, Vol. 21, 2009, pp. 1–16.
- ²³ Orth, R. C., Schetz, J. A., and Billig, F. S., “The Interaction and Penetration of Gaseous Jets in Supersonic Flow,” NASA CR-1386, July 1969.
- ²⁴ Spaid, F. W., and Cassel, L. A., “Aerodynamic Interference Induced by Reaction Controls,” AGARDograph No. 173, Dec. 1973.
- ²⁵ Salas, M. D., “The Numerical Calculation of Inviscid Plume Flow Fields,” AIAA Paper 1974-523, June 1974.
- ²⁶ Pai, S., *Fluid Dynamics of Jets*, 1st ed., Van Nostrand, New York, 1954.
- ²⁷ Chapman, D. R., Kuehn, D. M., and Larson, H. K., “Preliminary Report on a Study of Separated Flows in Supersonic and Subsonic Streams,” NACA RM A55L14, June 1956.
- ²⁸ “FUN3D Manual,” Oct. 2009, <http://fun3d.larc.nasa.gov> [retrieved Oct. 2009].
- ²⁹ Anderson, W.K. and Bonhaus, D.L., “An Implicit Upwind Algorithm for Computing Turbulent Flows on Unstructured Grids,” *Journal of Computational Physics*, Vol. 128, No. 2, 1996, pp. 391–408.
- ³⁰ Anderson, W. K., Rausch, R. D., and Bonhaus, D. L., “Implicit/Multigrid Algorithm for Incompressible Turbulent Flows on Unstructured Grids,” *Journal of Computational Physics*, Vol. 128, No. 2, 1996, pp. 391–408.
- ³¹ Edwards, J. R., “A Low-Diffusion Flux-Splitting Scheme for Navier-Stokes Calculations,” *Computers & Fluids*, Vol. 26, 1997, pp. 653–659.
- ³² Van Albada, G. D., B. Van Leer, B., and Roberts, W. W., “A Comparative Study of Computational Methods in Cosmic Gas Dynamics,” *Astron. Astrophysics*, Vol. 108, 1982, pp. 76.
- ³³ Menter, F. R., “Two-Equation Eddy-Viscosity Turbulence Models for Engineering Applications,” *AIAA Journal*, Vol. 32, No. 8, 1994, pp. 1598–1605.
- ³⁴ Peñaranda, F. E., and Freda, M. S., “Aeronautical Facilities Catalogue, Vol. 1 – Wind Tunnels”, NASA RP-1132, Jan. 1985.